Atomic Layer Engineering of Aluminum-Doped Zinc Oxide Films for Efficient and Stable Perovskite Solar Cells

Joanna Kruszyńska, Jakub Ostapko, Veysel Ozkaya, Belkis Surucu, Oliwia Szawcow, Kostiantyn Nikiforow, Marcin Hołdyński, Mohammad Mahdi Tavakoli, Pankaj Yadav, Małgorzata Kot, Grzegorz Piotr Kołodziej, Mateusz Wlazło, Soumitra Satapathi, Seckin Akin,* and Daniel Prochowicz*

Atomic layer deposition (ALD) has been considered as an efficient method to deposit high quality and uniform thin films of various electron transport materials for perovskite solar cells (PSCs). Here, the effect of deposition sequence in the ALD process of aluminum-doped zinc oxide (AZO) films on the performance and stability of PSCs is investigated. Particularly, the surface of AZO film is terminated by diethylzinc (DEZ)/H_2O (AZO-1) or trimethylaluminum (TMA)/H_2O pulse (AZO-2), and investigated with surface-sensitive X-ray photoelectron spectroscopy technique. It is observed that AZO-2 significantly enhances the thermal stability of the upcoming methylammonium lead iodide ($MAPbI_3$) layer and facilitates charge transport at the interface as evidenced by photoluminescence spectroscopes and favorable interfacial band alignment. Finally, planar-type PSC with AZO-2 layer exhibits a champion power conversion efficiency of 18.09% with negligible hysteresis and retains 82% of the initial efficiency after aging for 100 h under ambient conditions (relative humidity 40 ± 5%). These results highlight the importance of atomic layer engineering for developing efficient and stable PSCs.

1. Introduction

Over the last decade, photovoltaic technology has witnessed a rapid development of lead halide perovskites (LHPs) as promising light absorber materials, demonstrating low-cost solution processing, ease of fabrication, and outstanding optoelectronic properties.[1,2] Since the first report on the perovskite solar cells (PSCs) employing methylammonium lead iodide ($MAPbI_3$),[3] their power conversion efficiency (PCE) has now exceeded 25% for small-area cells.[4,5] The high efficiency of PSCs is achieved by tuning the perovskite layer through compositional engineering,[6–8] surface passivation,[9–13] and/or by using various additives.[14–16] Besides component engineering of the perovskite layer, a lot of works have been devoted to the development of efficient charge transport layers.[17–21] Particularly, the electron transport layers (ETLs) play an important role in realizing efficient and stable PSCs.[22,23] Thus far, titanium dioxide (TiO_2) is a widely applied ETL in PSCs but it suffers from low conductivity and high surface defect density.[24] Among alternative ETLs, zinc oxide (ZnO) has been regarded as a convenient candidate due to its high electron mobility and well-matched energy level with perovskite material.[25,26] This

J. Kruszyńska, K. Nikiforow, M. Hołdyński, D. Prochowicz
Institute of Physical Chemistry
Polish Academy of Sciences
Kasprzaka 44/52, Warsaw 01–224, Poland
E-mail: dprochowicz@ichf.edu.pl

J. Ostapko, O. Szawcow, G. P. Kołodziej, M. Wlazło
CBRTP – Research and Development Center of Technology for Industry
Waryńskiego 3A, Warsaw 00–645, Poland

V. Ozkaya, B. Surucu, S. Akin
Karamanoglu Mehmetbey University
Department of Metallurgical and Materials Engineering
Karaman 70100, Turkey
E-mail: seckinakin@kmu.edu.tr

M. M. Tavakoli
Department of Electrical Engineering and Computer Science
Massachusetts Institute of Technology
Cambridge, MA 02139, USA

P. Yadav
Department of Solar Energy
School of Technology
Pandit Deendayal Energy University
Gandhinagar, Gujarat 382 007, India

M. Kot
BTU COTTBUS – SENFTENBERG
Konrad-Zuse-Straße 1, 03046 Cottbus, Germany

S. Satapathi
Department of Physics
Indian Institute of Technology Roorkee
Roorkee, Haridwar, Uttarakhand 247667, India

**ADVANCED
SCIENCE NEWS**
www.advancedsciencenews.com

**ADVANCED
MATERIALS
INTERFACES**
www.advmatinterfaces.de

semiconducting ETL can be easily formed as a dense thin film layer through spin-coating of sol–gel or nanocrystals solution, chemical bath deposition, and magnetron sputtering.[27–29] However, regardless of the thin film formation method, the basic nature of ZnO was found to trigger the decomposition of the as-deposited MAPbI$_3$ layer during thermal treatment.[30–34] It has been proven that the deprotonation of the methylammonium cation and the formation of zinc hydroxide accelerate the perovskite decomposition.[35,36] To overcome this obstacle, the ZnO/perovskite interface instability can be mitigated by the interface passivation of the ZnO surface with various organic[33,34,37,38,39,40–42] or inorganic[14,43–48] modification layers, and doping of ZnO bulk with metal heteroatoms.[49–51] In the latter case, aluminum (Al) doping not only enhances the stability of the ZnO/perovskite interface by decreasing the basic property of ZnO[52] but also greatly improves its carrier concentration and electron mobility.[53] Thus, Al-doped zinc oxide (AZO) thin films have been reported to serve as a suitable ETL in PSCs. For example, Dong et al. revealed that the AZO film formed by spin-coating of Al(NO$_3$)$_3$ and Zn(OAc)$_2$ onto the ZnO nanorods suppresses the charge recombination at the interface and enhances the PCE up to 10.7%.[54] Mahmood et al. reported that the PCE of PSCs with AZO films deposited using the electrospraying method increases from 10.8% to 12.0%.[55] However, these deposition methods were not sufficient for compact film formation and precise thickness control, leading to a low PCE. Moreover, the thermal stability of the perovskite film on AZO formed by spin-coating commercially available AZO solution was strongly impacted as compared to the perovskite film deposited on SnO$_2$.[56] Therefore, it was highly desired to develop a synthetic strategy for depositing high-quality AZO film with better stability for the upcoming perovskite layer. In this context, atomic layer deposition (ALD) has been reported to form ultrathin and dense films in a precisely controlled way by controlling the number of specified reaction cycles between diethyl zinc (DEZ), water and trimethylaluminum (TMA).[57,58] The applications of ALD-AZO films in PSCs mostly concern examples where AZO was employed solely as the transparent conducting electrode[52,59,60] or is deposited on top of the perovskite layer.[18,61] However, the use of ALD-grown AZO as an ETL in the planar PSC architecture is relatively rare.[62] Moreover, the effect of the ALD parameters directly on the stability and quality of the upcoming perovskite coating has been rather unexplored.
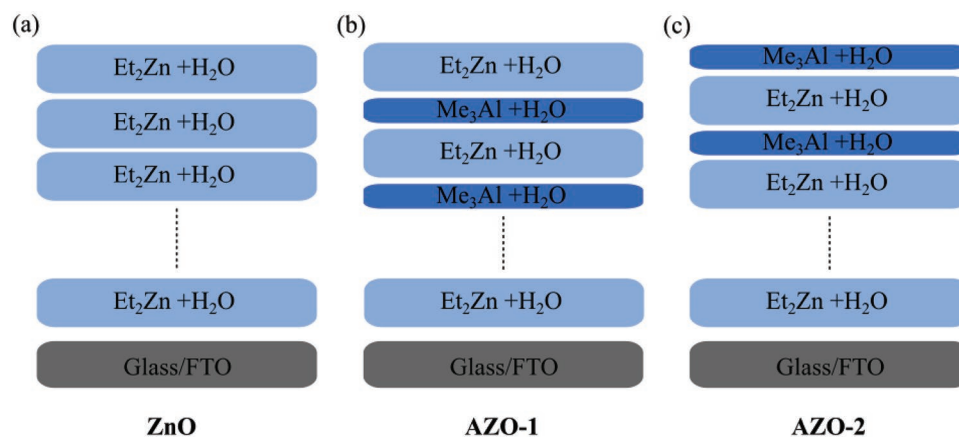
Herein, we demonstrate the effect of the ALD deposition sequence of AZO film on its optoelectronic properties and the film quality of the MAPbI$_3$ perovskite layer. Particularly, we find that the ending of the ALD process with the TMA/H$_2$O pulse lead to the formation of AZO film exhibiting superior electrical conductivity compared to the AZO ended with DEZ/H$_2$O pulse or pristine ZnO ETL. This modification not only improves the thermal stability and charge transfer of the ETL/perovskite interface but also shows favorable band energy alignment with the perovskite layer. As a result, our champion PSC results in a high PCE of 18.09% with alleviated hysteresis and improved environmental stability.

2. Results and Discussion

Scheme 1 shows the schematic representation of ALD processes for the formation of ZnO and AZO films. The growth per cycle (GPC) values for the deposition were calculated to be 0.165 and 3.12 nm per cycle for ZnO and AZO, respectively (see Tables S1–S3 in the Supporting Information for detailed information). The GPC values were used to estimate the number of macrocycles suitable for the formation of ≈20 nm thick layers. The reference ZnO thin films were synthesized by subsequently dosing diethylzinc (DEZ) and H$_2$O in 125 cycles (Scheme 1a). The conventional design strategy for ALD of AZO follows the process in which the single macrocycle is realized by the deposition of 19 layers of ZnO and one layer of AlO$_x$ by dosing the DEZ/H$_2$O and TMA/H$_2$O reagents, respectively (Scheme 1b). The macrocycle was repeated five times and then the film was terminated by deposition of 19 layers of ZnO, which led to the ZnO-terminated AZO (AZO-1). The AlO$_x$-terminated AZO (AZO-2) was synthesized by repeating the macrocycle 6 times, thereby the process was ended by deposition of single AlO$_x$ layer using TMA/H$_2$O reagents (Scheme 1c).

The formation of AZO-2 film is beneficial for the improvement of the surface conductivity and electron mobility as discussed below. All films were characterized by the four-point probe and the Hall-effect measurements, and the resulting electrical parameters are summarized in Table S4 in the Supporting

Scheme 1. Schematic representation of growth process of ZnO and AZO films by ALD.
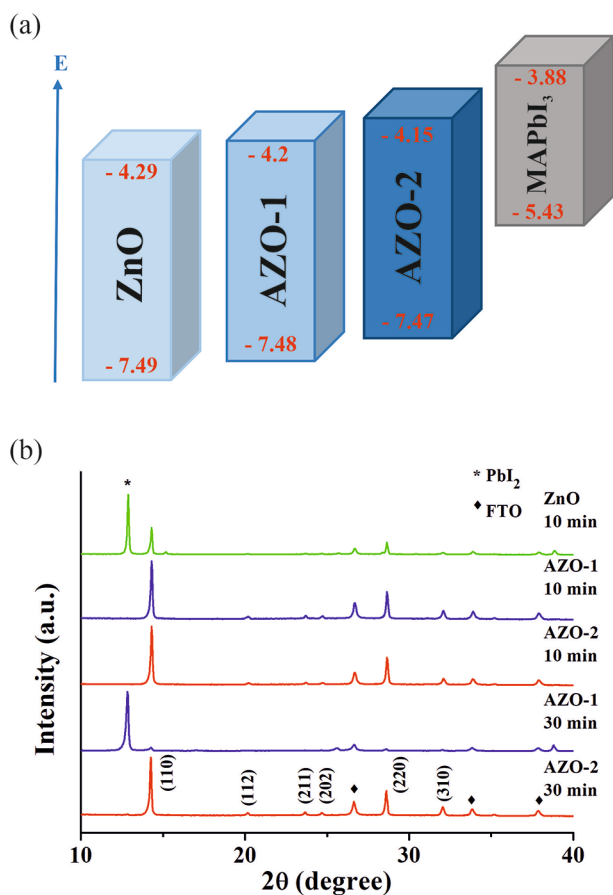
Figure 1. a) The schematic presentation of energy diagram for the ZnO, AZO-1, AZO-2 and MAPbI$_3$. b) XRD patterns of the perovskite films deposited on different ETLs and annealed at 100 °C at different times.

suggests changes in the bandgap to 3.28 and 3.32 eV, respectively.[65,66] Using bandgap data from the UV–vis and the valence bands values from UPS measurement, we estimated the conduction band energy levels of ZnO, AZO-1, and AZO-2 ETLs to be −4.29, −4.20, and 4.15 eV, respectively. Based on these calculations and the values from the literature,[67] we plotted the band diagram using these ETLs. As seen in the schematic of **Figure 1**a, the energy band offset between perovskite and AZO-2 is 270 meV, which is lower than the offset values for the AZO-1 (320 meV) and ZnO (410 meV) cases. As a result, the electron transfer from the perovskite layer to both AZO-1 and AZO-2 ETL can be facilitated compared with the ZnO ETL due to a better energy band alignment. Notably, AZO-2 shows even better band adjustment (lower energy band offset) with respect to the MAPbI$_3$ perovskite film. This can improve the charge transfer and reduce the interface recombination, resulting in a higher open circuit voltage (V_{OC}) and thus better efficiency in the PSCs.[68]

X-ray photoelectron spectroscopy (XPS) was used to probe the surface analysis of the resulting thin films (Figure S3, Supporting Information). In the ZnO film, the peak of Zn 2p$_{3/2}$ attributed to the crystalline lattice of zinc oxide is located at 1021.51 eV.[69] In the case of the AZO-1 and AZO-2 films, the Zn 2p$_{3/2}$ peak is very similar to the one observed in the ZnO sample with the positions of 1021.7 and 1021.6 eV, respectively. The O 1s XPS spectrum of ZnO ETL was deconvoluted into three peaks with energy levels of 530.2, 531.4, and 532.3 eV, which can be assigned to the lattice of oxygen atom in the Wurtzite structure of ZnO (peak A), the oxygen deficiency (peak B), and the hydroxyl groups on the ZnO surface (peak C), respectively.[70] The deconvolution of the O1s peak for AZO-1 and AZO-2 samples shows also a peak with the position of 533.2 eV (peak D), which can be assigned to the surface C–O– groups.[71] The appearance of a similar Al 2p peak centered at 74.3 eV in AZO-1 and AZO-2 films indicates the formation of Al–O bond within the original ZnO lattice through substitution of Zn^{2+} sites[72,73] rather than the formation of interface Al$_2$O$_3$ phase or metallic Al clusters during the ALD growth process.[74] Moreover, depth profiling measurement reveals that after removing the surface layer with the first few cycles of sputtering Al distribution in the bulk is constant, uniform, and similar for both samples (Figure S4, Supporting Information). Results of the quantitative analysis of the studied samples are presented in Table S6 in the Supporting Information. Carbon and carbon-bounded oxygen chemical states are not included in this analysis. As mentioned above, the O1s peak (peak A) at around 530.5 eV could be attributed to lattice oxygen atom, while the O1s peak (peak B) at higher binding energy (531.4 eV) is assigned to oxygen deficiency sites. Moreover, according to the literature data[75,76] the O^{2-} bounded with Al^{3+} is occupying the same position as O1s (peak B). Thus, in case of the AZO films both O^{2-} bounded with Al^{3+} and the one from ZnO deficiency sites contribute to the intensity of this peak. Those findings are in a good agreement with obtained data. In both AZO-1 and AZO-2 samples, contribution of the O1s peak (peak B) is higher (accordingly 11% at and 14% at) comparing to ZnO sample (7.9% at) reflecting the presence of the Al^{3+} in the samples. Worth noting that higher atomic concentration at the beginning of the sputtering of the Al^{3+} and higher contribution of the O1s peak (peak B) into the

Information. It is found that Al doping of ZnO reduces the thin film resistivity, and the conductivity parameter increases as follows: AZO-2 > AZO-1 > ZnO. According to the literature data,[63] the effect of Al-doping is attributed to the increase of carrier concentration, which is not fully suppressed by the reduction of mobility. However, the measured carrier mobility parameters for ZnO and AZO samples are increased upon Al doping. This effect, together with the increase of carrier concentration caused by Al doping, results in a remarkable reduction of the resistivity from 1.74 Ω cm for ZnO to 6.8 × 10^{-3} Ω cm for AZO-2. The effect of elevated mobility parameter upon Al doping has not been observed for much thicker AZO films[64] and maybe attributed to the ultrathin layer of studied materials and thickness-related defects.

Figure S1 in the Supporting Information shows the ultraviolet photoelectron spectroscopy (UPS) measurement of the ZnO, AZO-1, and AZO-2 films. Table S5 (Supporting Information) summarizes the values of the Fermi levels, valence bands, and conduction bands of these films extracted from the UPS and UV–vis results. The direct bandgap energy of the investigated films was extracted from the UV–vis absorption spectra (Figure S2, Supporting Information). The bandgap of the pristine ZnO is found to be 3.20 eV. However, the observed small blue shift of the AZO-1 and AZO-2 film absorption edges

oxygen atomic concentration in AZO-2 comparing to AZO-1 sample well-corresponded to the layer's deposition scheme ended with TMA/H$_2$O pulse. Average ratio of Al to Zn in bulk material obtained from XPS profiling of the samples is 0.067 ($\approx$1:15) for AZO-1 and 0.048 ($\approx$1:21) for AZO-2 (Figure S5, Supporting Information).

The subtle modification of a surface chemical state for the ETL can lead to a significant change in the stability of the ETL/perovskite interface. First, we tested the wettability of the investigated ETLs by contact angle measurements. Figure S6 (Supporting Information) shows the contact angle images of the corresponding ETL films after UV–O$_3$ treatment indicating a better wettability of AZO-1 and AZO-2 films for perovskite layer. Next, the thermal stability of the MAPbI$_3$ films deposited on different ETLs was studied. The films were annealed at 100 °C in argon glovebox at different times, and the color change in films was monitored as shown in Figure S7 in the Supporting Information. The MAPbI$_3$ film deposited on the ZnO substrate starts to decompose after 10 min of annealing, whereas the perovskite films deposited on AZO-1 and AZO-2 remained black during the applied heating time. The presence of perovskite structure was confirmed by the analysis of the X-ray diffraction (XRD) patterns, as shown in Figure 1b. The morphology of the perovskite films was analyzed by scanning electron microscopy (SEM). Top-view SEM images of all perovskite films reveal a compact morphology with no considerable difference in grains size (Figure S8, Supporting Information). The lack of defined grain boundaries observed in the perovskite film deposited on the ZnO layer indicates the degradation of the perovskite structure, which is well-corroborated with the XRD data. A prolonged heating time (30 min) starts degradation of

the MAPbI$_3$ film coated on top of AZO-1 as the presence of the characteristic peak around 12.5° in the XRD pattern suggests the formation of the PbI$_2$ phase. In turn, there is a small PbI$_2$ peak over this period for the MAPbI$_3$ film deposited on AZO-2 ETL, indicating an improved ETL/perovskite interface stability. Thus, the termination of the ALD process with TMA/H$_2$O pulse reduces the acid-base reaction between ZnO and MAPbI$_3$,[35] which results in better thermal stability of the perovskite layer.

The effect of ALD-deposited ETLs on the performance and stability of PSCs was further investigated by the fabrication of planar devices consisting of FTO/ETL/MAPbI$_3$/spiro-OMeTAD/Au (for device fabrication procedure see the Experimental Section). The perovskite films were spin-coated on different ETLs and annealed at 100 °C for only 10 min to avoid degradation. **Figure 2**a shows the current–voltage (J–V) curves of PSCs fabricated on different ETLs, and **Table 1** lists the collected photovoltaic (PV) parameters measured under AM 1.5G illumination and reverse scan. The ZnO-based device yields a champion PCE of 16.23% with a short-circuit current density (J$_{SC}$) of 22.82 mA cm^{-2}, an open-circuit voltage (V$_{OC}$) of 0.99 V, and a fill factor (FF) of 72%. In contrast, superior photovoltaic performance is observed for both AZO-based PSCs. While the AZO-1 device gives a PCE of 17.99% with a J$_{SC}$ of 23.20 mA cm^{-2}, V$_{OC}$ of 1.04 V, and FF of 74%, the device with AZO-2 offers the best PCE of 18.09% with a J$_{SC}$ of 23.16 mA cm^{-2}, V$_{OC}$ of 1.05 V, and FF of 74%. The integrated J$_{SC}$ values derived from external quantum efficiency (EQE) spectra well agree with the values of J$_{SC}$ obtained from J–V measurements (Figure 2b). The stabilized power output of these devices was monitored near the maximum power point under continuous illumination for 100 s (Figure 2c). The best AZO-2 device shows a steady-state
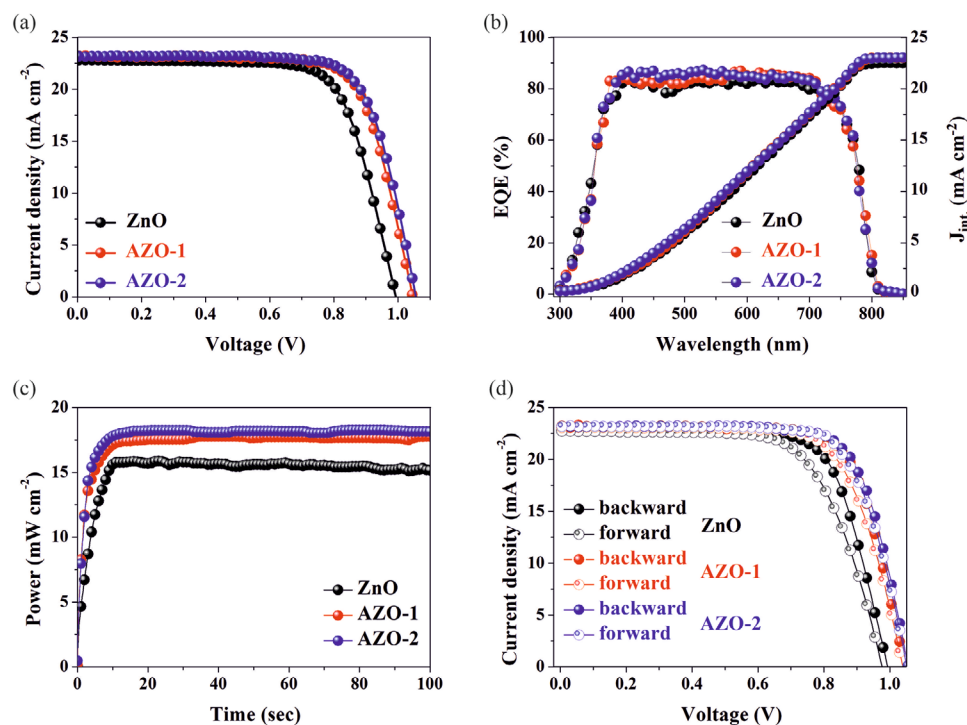

Figure 2. a) J–V curves of the best performing PSCs with different ETLs. b) EQE spectra of the devices based on the different ETLs. c) Steady state PCE of ZnO, AZO-1, and AZO-2 based devices. d) J–V curves of the devices under both forward (blank circles) and backward (filled circles) scan directions.

2200575 (4 of 8)

**ADVANCED
SCIENCE NEWS**

www.advancedsciencenews.com

**ADVANCED
MATERIALS
INTERFACES**

www.advmatinterfaces.de

Table 1. The photovoltaic (PV) parameters of the corresponding PSCs were measured under AM 1.5G illumination and reverse scan. The average data were collected from 8 devices for each ETL. The active area was set at 0.09 cm^2.

ETL		V_{OC} [V]	J_{SC} [mA cm^{-2}]	FF [%]	PCE [%]	J_{int} [mA cm^{-2}]
ZnO	champion	0.99	22.82	72	16.23	22.46
	average	0.98 ± 0.01	22.80 ± 0.08	69 ± 1.5	15.45 ± 0.41	
AZO-1	champion	1.04	23.20	74	17.99	22.97
	average	1.04 ± 0.01	23.17 ± 0.07	73 ± 1.1	17.65 ± 0.30	
AZO-2	champion	1.05	23.16	74	18.09	22.99
	average	1.05 ± 0.01	23.11 ± 0.05	74 ± 0.7	18.01 ± 0.20	

efficiency of 17.82%, which is among the highest efficiencies reported on AZO-based planar PSCs. We also examined the hysteresis of J–V curves of our devices based on different ETLs under reverse and forward scans (Figure 2d). The hysteresis index defined as [PCE$_{backward}$ − PCE$_{forward}$/PCE$_{forward}$ × 100] is found to be the lowest (1.29%) for AZO-2 device in comparison to that of AZO-1 (5.51%) and ZnO (9.22%) cells. The suppression of the hysteresis in the AZO-2 device can be attributed to improved charge transfer, as discussed further below.

The statistics of PV parameters from the collected individual devices are presented in Figure S9 in the Supporting Information. It is found that the high efficiency of AZO-2 devices is mainly due to the improvement in V_{OC} and FF parameters. The large V_{OC} is attributed to the favorable band alignment (Figure 1a) with respect to the perovskite layer, which reduces energy loss during charge transfer at the ETL/perovskite interface. To further study the charge transfer process at the interface

between ETL and perovskite, we performed steady-state photoluminescence (PL) and time-resolved PL (TRPL) measurements on the perovskite films deposited on different ETLs. **Figure 3**a shows the PL spectra of the corresponding perovskite films. It is found that the perovskite film coated on AZO-2 exhibits a significant PL quenching effect, indicating an improved charge collection at the interface. Figure 3b shows the normalized TRPL for the films deposited on different ETLs (for the fitting parameters see Table S7 in the Supporting Information). The perovskite film deposited on AZO-2 shows a carrier lifetime of 27 ns, which is shorter than that of AZO-1 (35 ns) and ZnO (58 ns) samples. The reduced carrier lifetime indicates more efficient charge transfer at the ETL/perovskite interface, which is consistent with the steady-state PL results.

The carrier recombination mechanism was also investigated by studying the V_{OC} dependencies under different light intensities for the resulted devices (Figure 3c). We used a formula
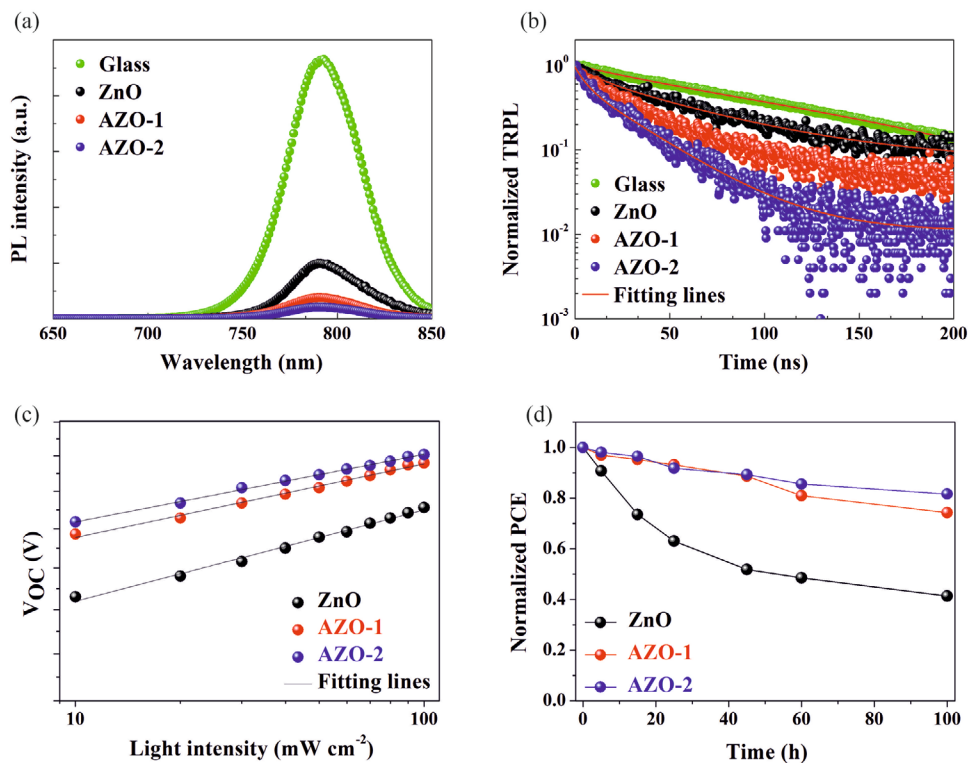

Figure 3. a) Steady-state PL and b) TRPL spectra of the perovskite films deposited on various ETLs. c) Measurement of V_{OC} as a function of illumination. d) Shelf-life stability test of the ZnO, AZO-1, and AZO-2 PSCs without encapsulation in ambient condition (relative humidity 40 ± 5%) for 100 h.

ADVANCED
SCIENCE NEWS
www.advancedsciencenews.com

ADVANCED
MATERIALS
INTERFACES
www.advmatinterfaces.de

of $V_{OC} = \frac{m_{\phi k_B} T}{q} \ln(\phi_{Ph})$ (where k_B is the Boltzmann constant, T is the thermodynamic temperature, and q is the electron charge) to unravel the trap-assisted recombination within the devices and the slopes are determined to be 1.94, 1.67, and 1.56 kT/q for devices based on ZnO, AZO-1, and AZO-2 ETLs, respectively. A lower value obtained for modified ETLs indicates a reduced trap-assisted recombination, inferring more effective charge transfer at ETL/perovskite interface. This result is also closely related and supportive with the increase in the V_{OC} value. The electrochemical impedance spectroscopy (EIS) was also employed to investigate the charge dynamics of the PSCs. Figure S10 (Supporting Information) shows the Nyquist plots of the devices based on different ETLs measured under dark near the V_{OC}. Two semicircles are observed for all devices in the frequency range of 1 Hz to 1 MHz. The semicircle at high-frequency is ascribed to the charge transfer resistance (R_{ct}), while the semicircle at low-frequency is in accordance with the recombination resistance (R_{rec}). As shown in Table S8 (Supporting Information), the R_{ct} values of the AZO-1 and AZO-2 ETL-based devices are lower than that of the ZnO counterpart, suggesting the conducing nature of Al doping. Similarly, the AZO-2 ETL-based device shows the highest R_{rec} value of 163 Ω, indicating a suppression in the charge carrier recombination, which arises from the reduced defect density. Moreover, the larger FF is ascribed to low R_s and high charge mobility of AZO-2, which could reduce the charge recombination.

We also monitored the shelf-stability of unencapsulated PSCs under ambient conditions (at room temperature with relative humidity (RH) of 40 ± 5%) for 100 h (Figure 3d). AZO-2 ETL-based device sustained 82% of its initial PCE after aging for 100 h, while the ZnO-based device reveals two-fold quicker degradation up to 41% of its initial PCE under the same storage conditions. The improved stability of the AZO-2 device is associated with the enhanced ETL/perovskite interface stability.

3. Conclusions

In summary, we demonstrated that a subtle tuning of the ALD deposition sequence during the formation of AZO film plays a beneficial role on the properties of the upcoming perovskite film and performance of the solar cell devices. The controlled termination of the ALD process with TMA/H_2O pulse not only offers high conductivity for the AZO film but also leads to the favorable band alignment concerning the perovskite layer, which facilitates charge transfer at the interface. In addition, the above modification of a surface chemical state of AZO film prevents the degradation reaction at the ETL/perovskite interface and improves the thermal stability of the MAPbI$_3$ film compared to the control perovskite films deposited on the AZO terminated with DEZ/H_2O pulse and ZnO ETLs. Consequently, our best planar device yielded a high PCE of 18.09% (stabilized at 17.82%) with negligible hysteresis. Moreover, the environmental stability of the optimized device is improved by retaining 82% of its initial PCE after aging for 100 h at ambient conditions. These results demonstrate the superiority of the developed atomic layer engineering approach that may open up new possibilities for the design of efficient AZO-based ETLs to tackle the thermal instability issue of the ZnO/perovskite

interface and offer a new direction for the fabrication of highly efficient PSCs.

4. Experimental Section

Materials: All perovskite materials: methylammonium iodide (MAI), lead iodide (PbI$_2$), 2,2″,7,7″-Tetrakis[N,N-di(4-methoxyphenyl)amino]-9,9′-spirobifluorene (spiro-OMeTAD), 4-tertbutylpyridine (TBP), and lithium bis-(trifluoromethylsulphonyl)imide (Li-TFSI)) are received from Sigma-Aldrich.

ETL Film Formation and Characterization: ALD-grown thin films were deposited at 200 °C using Beneq P400A ALD reactor. Borosilicate glass, quartz slides (Continental Trade), FTO covered glass slides (Biotain Crystal) and polished silicon wafers (Sieger Wafer) were used as substrates for the film growth. The deposition processes were carried out using nitrogen as a carrier gas at 2500 sccm flow, which corresponds to the 0.8 hPa pressure. Diethyl zinc (DEZ, Lanxess), TMA (Lanxess), and deionized water were used as zinc, aluminum, and oxygen sources, respectively. For the deposition of zinc oxide, the sequence of dosing and purging pulses was as follow, ZnO: [H_2O] + [N_2] + [DEZ] + [N_2] + [H_2O] with H_2O and DEZ dosing times 0.35 s and nitrogen purging time equal to 3.0 s. The aluminum oxide was deposited according to the sequence AlO$_x$: [H_2O] + [N_2] + [TMA] + [N_2] + [H_2O] with H_2O and TMA dosing time 0.35 s and nitrogen purging time equal to 3.0 s. The AZO thin films were deposited using previously optimized pulses ratio corresponding to the minimal film resistivity [DEZ]/[TMA] = 19, according to the scheme: $n \times (19 \times ZnO + 1 \times AlO_x) + 19 \times ZnO$, where the n is the number of cycles. For the deposition of AZO thin films terminated by the AlO$_x$ species, the deposition scheme was ended with TMA and H_2O pulses, according to the scheme: $n \times (19 \times ZnO + 1 \times AlO_x)$. The thickness of deposited films was measured on polished-Si deposited samples using Filmetrics F20 reflectometer. The sample resistivity was measured using Ossila four-point probe on samples deposited on borosilicate glass. Hall measurements were carried out using HMS-5500, Bridge Technology instrument, at room temperature.

X-ray photoelectron spectroscopic (XPS) measurements were performed by a ULVAC-PHI VersaProbe 5000 spectrometer using monochromatic Al Ka radiation ($h = 1486.6$ eV). X-ray source operates at 100 µm spot size, 25 W power, and 15 kV acceleration voltage. The Multipak and CasaXPS software were used to evaluate the obtained data. The binding energy (BE) scale refers to the Fermi level and was adjusted to the carbon XPS peak position (C 1s – at the binding energy of 284.8 eV). The distribution of the elements within the ALD layers was investigated using the XPS technique combined with Ar$^+$ depth profile sputtering. XPS depth profiles were cycled with Ar$^+$ bombardment with 1 kV ion beam for 1 min. Cycles were repeated until a signal from the glass substrate was observed. The top-view images of the perovskite films were assessed by field emission scanning electron microscopy (FE-SEM) (S5500, Hitachi). UV–vis spectra were obtained using Thermo Scientific Evolution 220 instrument. The band energy levels of ETLs were studied by UPS (XPS-ASAM with detector DLSEGD-Phoibos-Hsa3500). The contact angle measurements were assessed by a drop shape analyzer (KRUSS, DSA100) at ambient temperature.

Solar Cell Preparation: The patterned fluorine-doped tin oxide (FTO) glass was cleaned using Hellmanex detergent in deionized water, acetone, and isopropanol for 20 min each, respectively. The ETL films were prepared according to the procedure above. A perovskite precursor composition of MAPbI$_3$ was spin-coated on the corresponding ETLs at 1000 and 4000 rpm for 10 and 20 s, respectively. 100 µL of chlorobenzene was dripped at the 10 s before the end of the last step. After that, the films were sequentially annealed at 65 °C for 1 min and 100 °C for 10 min. Next, ≈70 × 10^{-3} M spiro-OMeTAD was prepared in chlorobenzene by adding TBP and Li-TFSI in acetonitrile (molar ratio of spiro-OMeTAD:Li-TFSI:TBP of 1:0.5:3.3) and deposited on top of the perovskite films by spin-coating at 4000 rpm for 20 s. Finally, ≈80 nm of the gold electrode was evaporated using thermal evaporation under high vacuum. The active area was set at 0.09 cm^2.

**ADVANCED
SCIENCE NEWS**

www.advancedsciencenews.com

**ADVANCED
MATERIALS
INTERFACES**

www.advmatinterfaces.de

Device Measurement and Characterization: The photovoltaic parameters of devices were defined with the power source meter (Keithley 2400), using a 450 W Xenon light source from Oriel with an AM 1.5 filter. The external quantum efficiency (EQE) analysis was performed with a light-emitting-diode (LED) light source (Enli-Tech). The electrochemical impedance spectroscopy (EIS) measurements were measured by a potentiostat (Ivium) under dark near the V_{OC}. For the stability test, unencapsulated cells were stored under ambient conditions at relative humidity (R.H.) of 40%. The performance of the cells was periodically measured under simulated sunlight. XRD data of the perovskite films prior stability measurement were collected on the Empyrean diffractometer (PANalytical). The PL spectra of perovskite films were recorded with a spectrometer (Hitachi).

Supporting Information

Supporting Information is available from the Wiley Online Library or from the author.

Conflict of Interest

The authors declare no conflict of interest.

Data Availability Statement

The data that support the findings of this study are available from the corresponding author upon reasonable request.

[1] A. K. Jena, A. Kulkarni, T. Miyasaka, *Chem. Rev.* **2019**, *119*, 3036.
[2] S. Sahare, H. D. Pham, D. Angmo, P. Ghoderao, J. MacLeod, S. B. Khan, S. Lee, S. P. Singh, P. Sonar, *Adv. Energy Mater.* **2021**, *11*, 2101085.
[3] A. Kojima, K. Teshima, Y. Shirai, T. Miyasaka, *J. Am. Chem. Soc.* **2009**, *131*, 6050.
[4] J. Jeong, M. Kim, J. Seo, H. Lu, P. Ahlawat, A. Mishra, Y. Yang, M. A. Hope, F. T. Eickemeyer, M. Kim, Y. J. Yoon, I. W. Choi, B. P. Darwich, S. J. Choi, Y. Jo, J. H. Lee, B. Walker, S. M. Zakeeruddin, L. Emsley, U. Rothlisberger, A. Hagfeldt, D. S. Kim, M. Grätzel, J. Y. Kim, *Nature* **2021**, *592*, 381.
[5] H. Min, D. Y. Lee, J. Kim, G. Kim, K. S. Lee, J. Kim, M. J. Paik, Y. K. Kim, K. S. Kim, M. G. Kim, T. J. Shin, S. Il Seok, *Nature* **2021**, *598*, 444.
[6] N. J. Jeon, J. H. Noh, W. S. Yang, Y. C. Kim, S. Ryu, J. Seo, S. I. Seok, *Nature* **2015**, *517*, 476.
[7] N. Park, *Adv. Energy Mater.* **2020**, *10*, 1903106.
[8] D. Prochowicz, R. Runjhun, M. M. Tavakoli, P. Yadav, M. Saski, A. Q. Alanazi, D. J. Kubicki, Z. Kaszkur, S. M. Zakeeruddin, J. Lewiński, M. Grätzel, *Chem. Mater.* **2019**, *31*, 1620.
[9] Y. Bai, S. Xiao, C. Hu, T. Zhang, X. Meng, H. Lin, Y. Yang, S. Yang, *Adv. Energy Mater.* **2017**, *7*, 1701038.
[10] Q. Jiang, Y. Zhao, X. Zhang, X. Yang, Y. Chen, Z. Chu, Q. Ye, X. Li, Z. Yin, J. You, *Nat. Photonics* **2019**, *13*, 460.
[11] L. Fu, H. Li, L. Wang, R. Yin, B. Li, L. Yin, *Energy Environ. Sci.* **2020**, *13*, 4017.
[12] E. Akman, S. Akin, *Adv. Mater.* **2021**, *33*, 2006087.
[13] J. Wang, G. Jin, Q. Zhen, C. He, Y. Duan, *Adv. Mater. Interfaces* **2021**, *8*, 2002078.
[14] F. Zhang, K. Zhu, *Adv. Energy Mater.* **2019**, *10*, 1902579.
[15] A. Mahapatra, D. Prochowicz, M. M. Tavakoli, S. Trivedi, P. Kumar, P. Yadav, *J. Mater. Chem. A* **2020**, *8*, 27.
[16] S. Akin, E. Akman, S. Sonmezoglu, *Adv. Funct. Mater.* **2020**, *30*, 2002964.
[17] S. S. Shin, S. J. Lee, S. I. Seok, *Adv. Funct. Mater.* **2019**, *29*, 1900455.
[18] S. Seo, S. Jeong, C. Bae, N.-G. Park, H. Shin, *Adv. Mater.* **2018**, *30*, 1801010.
[19] G. Kim, H. Choi, M. Kim, J. Lee, S. Y. Son, T. Park, *Adv. Energy Mater.* **2020**, *10*, 1903403.
[20] S. Akin, *ACS Appl. Mater. Interfaces* **2019**, *11*, 39998.
[21] F. Sadegh, S. Akin, M. Moghadam, V. Mirkhani, M. A. Ruiz–Preciado, Z. Wang, M. M. Tavakoli, M. Graetzel, A. Hagfeldt, W. Tress, *Nano Energy* **2020**, *75*, 105038.
[22] J. Lian, B. Lu, F. Niu, P. Zeng, X. Zhan, *Small Methods* **2018**, *2*, 1800082.
[23] S. Sonmezoglu, S. Akin, *Nano Energy* **2020**, *76*, 105127.
[24] Y. Zhu, K. Deng, H. Sun, B. Gu, H. Lu, F. Cao, J. Xiong, L. Li, *Adv. Sci.* **2018**, *5*, 1700614.
[25] P. Tiwana, P. Docampo, M. B. Johnston, H. J. Snaith, L. M. Herz, *ACS Nano* **2011**, *5*, 5158.
[26] Z. Cao, C. Li, X. Deng, S. Wang, Y. Yuan, Y. Chen, Z. Wang, Y. Liu, L. Ding, F. Hao, *J. Mater. Chem. A* **2020**, *8*, 19768.
[27] D. Liu, T. L. Kelly, *Nat. Photonics* **2014**, *8*, 133.
[28] P. Zhang, J. Wu, T. Zhang, Y. Wang, D. Liu, H. Chen, L. Ji, C. Liu, W. Ahmad, Z. D. Chen, S. Li, *Adv. Mater.* **2018**, *30*, 1703737.
[29] H. Niu, C. Fang, X. Wei, H. Wang, L. Wan, Y. Li, X. Mao, J. Xu, R. Zhou, *Dalton Trans.* **2021**, *50*, 6477.
[30] Y. Cheng, Q.-D. Yang, J. Xiao, Q. Xue, H.-W. Li, Z. Guan, H.-L. Yip, S.-W. Tsang, *ACS Appl. Mater. Interfaces* **2015**, *7*, 19986.
[31] J. Yang, B. D. Siempelkamp, E. Mosconi, F. De Angelis, T. L. Kelly, *Chem. Mater.* **2015**, *27*, 4229.
[32] Y. Dkhissi, S. Meyer, D. Chen, H. C. Weerasinghe, L. Spiccia, Y.-B. Cheng, R. A. Caruso, *ChemSusChem* **2016**, *9*, 687.
[33] M. M. Tavakoli, R. Tavakoli, P. Yadav, J. Kong, *J. Mater. Chem. A* **2019**, *7*, 679.
[34] M. M. Tavakoli, R. Tavakoli, Z. Nourbakhsh, A. Waleed, U. S. Virk, Z. Fan, *Adv. Mater. Interfaces* **2016**, *3*, 1500790.
[35] K. Schutt, P. K. Nayak, A. J. Ramadan, B. Wenger, Y. Lin, H. J. Snaith, *Adv. Funct. Mater.* **2019**, *29*, 1900466.
[36] S. Tsarev, S. Olthof, A. G. Boldyreva, S. M. Aldoshin, K. J. Stevenson, P. A. Troshin, *Nano Energy* **2021**, *83*, 105774.
[37] L. Zuo, Z. Gu, T. Ye, W. Fu, G. Wu, H. Li, H. Chen, *J. Am. Chem. Soc.* **2015**, *137*, 2674.
[38] Q. An, P. Fassl, Y. J. Hofstetter, D. Becker-Koch, A. Bausch, P. E. Hopkinson, Y. Vaynzof, *Nano Energy* **2017**, *39*, 400.

[39] D. Liu, Y. Wang, Z. She, H. Zheng, P. Zhang, F. Wang, J. Wu, Z. Chen, S. Li, *Sol. RRL* **2018**, *2*, 1800240.

[40] C. Liu, D. Zhang, Z. Li, W. Han, G. Ren, Z. Li, L. Shen, W. Guo, W. Zheng, *Sol. RRL* **2020**, *4*, 1900489.

[41] J. Han, H. Kwon, E. Kim, D.-W. Kim, H. J. Son, D. H. Kim, *J. Mater. Chem. A* **2020**, *8*, 2105.

[42] C. Liu, W. Wu, D. Zhang, Z. Li, G. Ren, W. Han, W. Guo, *J. Mater. Chem. A* **2021**, *9*, 12161.

[43] R. Chen, J. Cao, Y. Duan, Y. Hui, T. T. Chuong, D. Ou, F. Han, F. Cheng, X. Huang, B. Wu, N. Zheng, *J. Am. Chem. Soc.* **2019**, *141*, 541.

[44] J. Cao, B. Wu, R. Chen, Y. Wu, Y. Hui, B.-W. Mao, N. Zheng, *Adv. Mater.* **2018**, *30*, 1705596.

[45] Tulus, S. Olthof, M. Marszalek, A. Peukert, L. A. Muscarella, B. Ehrler, O. Vukovic, Y. Galagan, S. C. Boehme, E. von Hauff, *ACS Appl. Energy Mater.* **2019**, *2*, 3736.

[46] S. S. Mali, J. V. Patil, C. K. Hong, *Adv. Energy Mater.* **2020**, *10*, 1902708.

[47] J. Ma, Z. Lin, X. Guo, L. Zhou, J. Su, C. Zhang, Z. Yang, J. Chang, S. (Frank) Liu, Y. Hao, *Sol. RRL* **2019**, *3*, 1900096.

[48] M. M. Tavakoli, H. T. Dastjerdi, P. Yadav, D. Prochowicz, H. Si, R. Tavakoli, *Adv. Funct. Mater.* **2021**, *31*, 2010623.

[49] Z.-L. Tseng, C.-H. Chiang, S.-H. Chang, C.-G. Wu, *Nano Energy* **2016**, *28*, 311.

[50] J. Song, E. Zheng, L. Liu, X. Wang, G. Chen, W. Tian, T. Miyasaka, *ChemSusChem* **2016**, *9*, 2640.

[51] R. Azmi, S. Hwang, W. Yin, T.-W. Kim, T. K. Ahn, S.-Y. Jang, *ACS Energy Lett.* **2018**, *3*, 1241.

[52] X. Zhao, H. Shen, Y. Zhang, X. Li, X. Zhao, M. Tai, J. Li, J. Li, X. Li, H. Lin, *ACS Appl. Mater. Interfaces* **2016**, *8*, 7826.

[53] K. Mahmood, S. B. Park, *Electron. Mater. Lett.* **2013**, *9*, 161.

[54] J. Dong, Y. Zhao, J. Shi, H. Wei, J. Xiao, X. Xu, J. Luo, J. Xu, D. Li, Y. Luo, Q. Meng, *Chem. Commun.* **2014**, *50*, 13381.

[55] K. Mahmood, B. S. Swain, H. S. Jung, *Nanoscale* **2014**, *6*, 9127.

[56] M. Spalla, E. Planes, L. Perrin, M. Matheron, S. Berson, L. Flandin, *ACS Appl. Energy Mater.* **2019**, *2*, 7183.

[57] M.-L. Lin, J.-M. Huang, C.-S. Ku, C.-M. Lin, H.-Y. Lee, J.-Y. Juang, *J. Alloys Compd.* **2017**, *727*, 565.

[58] Z. Xing, J. Xiao, T. Hu, X. Meng, D. Li, X. Hu, Y. Chen, *Small Methods* **2020**, *4*, 2000588.

[59] A. S. Chouhan, N. P. Jasti, S. Avasthi, *Org. Electron.* **2019**, *66*, 249.

[60] X. Li, W. Ye, X. Zhou, F. Huang, D. Zhong, *J. Phys. Chem. C* **2017**, *121*, 10282.

[61] K. O. Brinkmann, T. Gahlmann, T. Riedl, *Sol. RRL* **2020**, *4*, 1900332.

[62] A. F. Palmstrom, G. E. Eperon, T. Leijtens, R. Prasanna, S. N. Habisreutinger, W. Nemeth, E. A. Gaulding, S. P. Dunfield, M. Reese, S. Nanayakkara, T. Moot, J. Werner, J. Liu, B. To, S. T. Christensen, M. D. McGehee, M. F. A. M. van Hest, J. M. Luther, J. J. Berry, D. T. Moore, *Joule* **2019**, *3*, 2193.

[63] G. Luka, T. A. Krajewski, B. S. Witkowski, G. Wisz, I. S. Virt, E. Guziewicz, M. Godlewski, *J. Mater. Sci.: Mater. Electron.* **2011**, *22*, 1810.

[64] P. Banerjee, W. J. Lee, K. R. Bae, S. B. Lee, G. W. Rubloff, *J. Appl. Phys.* **2010**, *108*, 043504.

[65] A. Wang, T. Chen, S. Lu, Z. Wu, Y. Li, H. Chen, Y. Wang, *Nanoscale Res. Lett.* **2015**, *10*, 75.

[66] P. Mbule, D. Wang, R. Grieseler, P. Schaaf, B. Muhsin, H. Hoppe, B. Mothudi, M. Dhlamini, *Sol. Energy* **2018**, *172*, 219.

[67] C.-C. Chueh, C.-Z. Li, A. K.-Y. Jen, *Energy Environ. Sci.* **2015**, *8*, 1160.

[68] M. M. Tavakoli, P. Yadav, R. Tavakoli, J. Kong, *Adv. Energy Mater.* **2018**, *8*, 1800794.

[69] G. H. Mhlongo, D. E. Motaung, I. Kortidis, N. R. Mathe, O. M. Ntwaeaborwa, H. C. Swart, B. W. Mwakikunga, S. S. Ray, G. Kiriakidis, *Mater. Chem. Phys.* **2015**, *162*, 628.

[70] D. Zheng, G. Wang, W. Huang, B. Wang, W. Ke, J. L. Logsdon, H. Wang, Z. Wang, W. Zhu, J. Yu, M. R. Wasielewski, M. G. Kanatzidis, T. J. Marks, A. Facchetti, *Adv. Funct. Mater.* **2019**, *29*, 1900265.

[71] A. P. Terzyk, *Colloids Surf., A* **2001**, *177*, 23.

[72] Y. Li, R. Yao, H. Wang, X. Wu, J. Wu, X. Wu, W. Qin, *ACS Appl. Mater. Interfaces* **2017**, *9*, 11711.

[73] Z. Chen, G. Zhan, Y. Wu, X. He, Z. Lu, *J. Alloys Compd.* **2014**, *587*, 692.

[74] C. J. Powell, A. V. Naumkin, A. Kraut-Vass, S. W. Gaarenstroom, *NIST X-ray Photoelectron Spectroscopy Database, NIST Standard Reference Database 20, Version 4.1* **2012**, https://doi.org/10.18434/T4T88K.

[75] H. He, K. Alberti, T. L. Barr, J. Klinowski, *J. Phys. Chem.* **1993**, *97*, 13703.

[76] A. M. Venezia, R. Bertoncello, G. Deganello, *Surf. Interface Anal.* **1995**, *23*, 239.